

Spectral variability of the blazar 3C 279 in the optical to X-ray band during 2009–2018

SUNGMIN YOO AND HONGJUN AN¹¹*Department of Astronomy and Space Science, Chungbuk National University, Cheongju, 28644, Republic of Korea*

ABSTRACT

We report on spectral variability of the blazar 3C 279 in the optical to X-ray band between MJD 55100 and 58400 during which long-term radio variability was observed. We construct light curves and band spectra in each of the optical (2×10^{14} – 1.5×10^{15} Hz) and X-ray (0.3–10 keV) bands, measure the spectral parameters (flux F and spectral index α), and investigate correlation between F and α within and across the bands. We find that the correlation of the optical properties dramatically change after \sim MJD 55500 and the light curves show more frequent activity after \sim MJD 57700. We therefore divide the time interval into three “states” based on the correlation properties and source activity in the light curves, and analyze each of the three states separately. We find various correlations between the spectral parameters in the states and an intriguing 65-day delay of the optical emission with respect to the X-ray one in state 2 (MJD 55500–57700). We attempt to explain these findings using a one-zone synchro-Compton emission scenario.

Keywords: Active galactic nuclei (16), High energy astrophysics (739), Blazars (164), Spectral energy distribution (2129)

1. INTRODUCTION

Blazars, the most energetic radiation sources in the Universe, are active galactic nuclei (AGNs) with one of the jets pointing toward Earth (Urry & Padovani 1995). Their large energy output is believed to be produced in the central region by rapid spin of a supermassive black hole (Blandford & Znajek 1977) and flows outwards in the form of bipolar jets. The relativistic particles in the jets produce radiation which is further boosted due to Doppler beaming, and so blazars are bright across the entire electromagnetic wavebands.

As bright blazars can be seen even at very high redshifts ($z > 5$; Romani et al. 2004), they are very useful to study environments in the early Universe and its Cosmic evolution (e.g., H. E. S. S. Collaboration et al. 2013). Furthermore, blazars are energetically favorable sources of ultra high-energy Cosmic rays (UHE-CRs) and neutrinos, and can give us important clues to the acceleration mechanisms of the $> 10^{15}$ eV particles (e.g., Rodrigues et al. 2018). These studies require detailed knowledge on the spectral energy distribution (SED) of blazars’ emission for making beaming correc-

tion (e.g., An & Romani 2018), characterizing absorption by the extragalactic background light (EBL; e.g., Ackermann et al. 2016), and constraining the jet contents (e.g., Böttcher et al. 2013).

Blazars’ emission SEDs are phenomenologically well characterized by double-hump structure: a low-energy hump in the optical to X-ray band and a high-energy one in the X-ray to gamma-ray band. The low-energy hump is believed to be produced by synchrotron radiation of electrons, and the high-energy one by inverse-Compton (IC) upscattering of internal (synchrotron-self-Compton; SSC) or external (external Compton; EC) soft-photon fields (e.g., Dermer 1995). It was also suggested that additional hadronic contributions could be important in some blazars (e.g., Böttcher et al. 2013; Bottacini et al. 2016). Note that low-frequency radio photons are self-absorbed (synchrotron-self-absorption; SSA) in the compact high-energy emitting jets, and so the observed radio photons are believed to be emitted further downstream of the jet in these models.

This one-zone picture cannot explain all the diverse phenomena observed in blazars’ emission but captures main features of the blazar SEDs. More complicated models (e.g., MacDonald et al. 2015) were also developed and applied to some blazars with limited success. Nevertheless, particle acceleration mechanisms, structure of the jet flow, and the composition of the jets are

Corresponding author: Hongjun An
hjan@cbnu.ac.kr

Table 1. Observational data used in this work

Instrument	Band	Refs.
OVRO	15 GHz	https://www.astro.caltech.edu/ovroblazars/
WISE	Bands 1–4	https://www.nasa.gov/mission_pages/WISE/main/index.html
Steward	VR	http://james.as.arizona.edu/~psmith/Fermi/
SMARTS	BVRJ	http://www.astro.yale.edu/smarts/glast/home.php
Swift/UVOT	170–600 nm	https://swift.gsfc.nasa.gov/
Swift/XRT	0.3–10 keV	https://swift.gsfc.nasa.gov/

not yet very well known. Because the emission mechanisms for the two SED humps differ, the frequency and time dependence of their variability induced by jet activities can give us crucial information on the jet structure and particle acceleration mechanisms. These have been studied by SED modeling and multi-wavelength variability analyses (e.g., Paliya et al. 2015; Liodakis et al. 2018).

3C 279 is a very bright and highly variable blazar ($z = 0.536$; Marziani et al. 1996), and is categorized as a flat-spectrum radio quasar (FSRQ). It exhibits complex multi-wavelength variabilities: long-term (years) radio variability, short-term (days) optical and X-ray flares, and minute-scale gamma-ray flares (e.g., Hayashida et al. 2015). Some of these flares show correlation in multiple wavebands (e.g., Patiño-Álvarez et al. 2018; Beaklini et al. 2019; Larionov et al. 2020; Prince 2020). As such, 3C 279 can give us insights into blazar jet physics with its rich temporal and spectral properties. In this paper, we present our spectral variability studies performed using ~ 9 -yr observations in the optical to X-ray band.

2. DATA REDUCTION AND ANALYSIS

In order to construct band spectra in each of the optical (2×10^{14} – 1.5×10^{15} Hz) and X-ray (0.3–10 keV) bands, high-cadence nearly contemporaneous multi-frequency data are needed. We therefore analyze data taken with the *Neil-Gehrels-Swift* satellite, and supplement these with data taken from public catalogs. The data used in this work are listed in Table 1.

2.1. Swift data analysis

Since 3C 279 was monitored frequently with the *Neil-Gehrels-Swift* observatory, it provides relatively high-cadence data in the X-ray (0.3–10 keV; XRT) and six optical bands (170–600 nm; UVOT). We download the observational data in the HEASARC data archive and use the UVOT and XRT data for our studies.

For the UVOT data analysis, we use an $R = 5''$ circular and an $R = 20 - 30''$ annular regions centered at 3C 279 for the source and background, respectively. We then measure the source flux using the `uvotsource` tool integrated in HEASOFT v6.22.

For the XRT data, we first reprocess the data using `xrtpipeline` to produce cleaned event files. We then perform a spectral analysis using $R = R_{\text{in}} - 70''$ (with R_{in} varying depending on the degree of pile up) and $R = 120 - 210''$ annular regions for the source and background, respectively. Note that photon pile-up occurred in some of the observations because of X-ray flares of 3C 279 (see also Larionov et al. 2020). In this case, we further inspect the event distribution and excise central regions affected by pile-up.¹ The corresponding ancillary files are produced with `xrtmkarf`, and we use pre-computed redistribution matrix files (RMFs). We then fit the spectra with power-law models (`tbabs*pow`) holding N_{H} fixed at $2.2 \times 10^{20} \text{ cm}^{-2}$ in XSPEC 12.9.1p to measure the source flux and produce the X-ray light curve. For the absorption model, we use `vern` cross section (Verner et al. 1996) and `angr` abundance (Anders & Grevesse 1989). The fits are well acceptable with the typical $\chi^2/\text{dof}=0.98$. The resulting light curve is shown in Figure 1. Note that the *Swift* data used in this work were also analyzed and presented previously (e.g., Larionov et al. 2020; Prince 2020), but we carry out more detailed ‘spectral’ studies in this paper.

2.2. Public catalog data

Swift UVOT provides optical data with reasonable quality but the cadence is insufficient for our studies; other data are necessary to cover the gaps. So we supplement the UVOT data with the public SMARTS- and Steward-catalog ones (Table 1; Smith et al. 2009; Bonning et al. 2012). We correct the optical data for Galactic extinction using A_{λ} values found in NED² (Schlafly & Finkbeiner 2011), convert the magnitude into flux units (Bessell et al. 1998) and generate light curves. Note that some of the data were also presented in previous works (e.g., Paliya et al. 2015; Patiño-Álvarez et al. 2018; Larionov et al. 2020; Prince 2020). We also use limited *WISE* observations ($\sim 10^{13}$ – 10^{14} Hz) here; these are not used for band spectral fits but for qualitative characterization of the SEDs. We also

¹ <https://www.swift.ac.uk/analysis/xrt/pileup.php>

² https://ned.ipac.caltech.edu/extinction_calculator

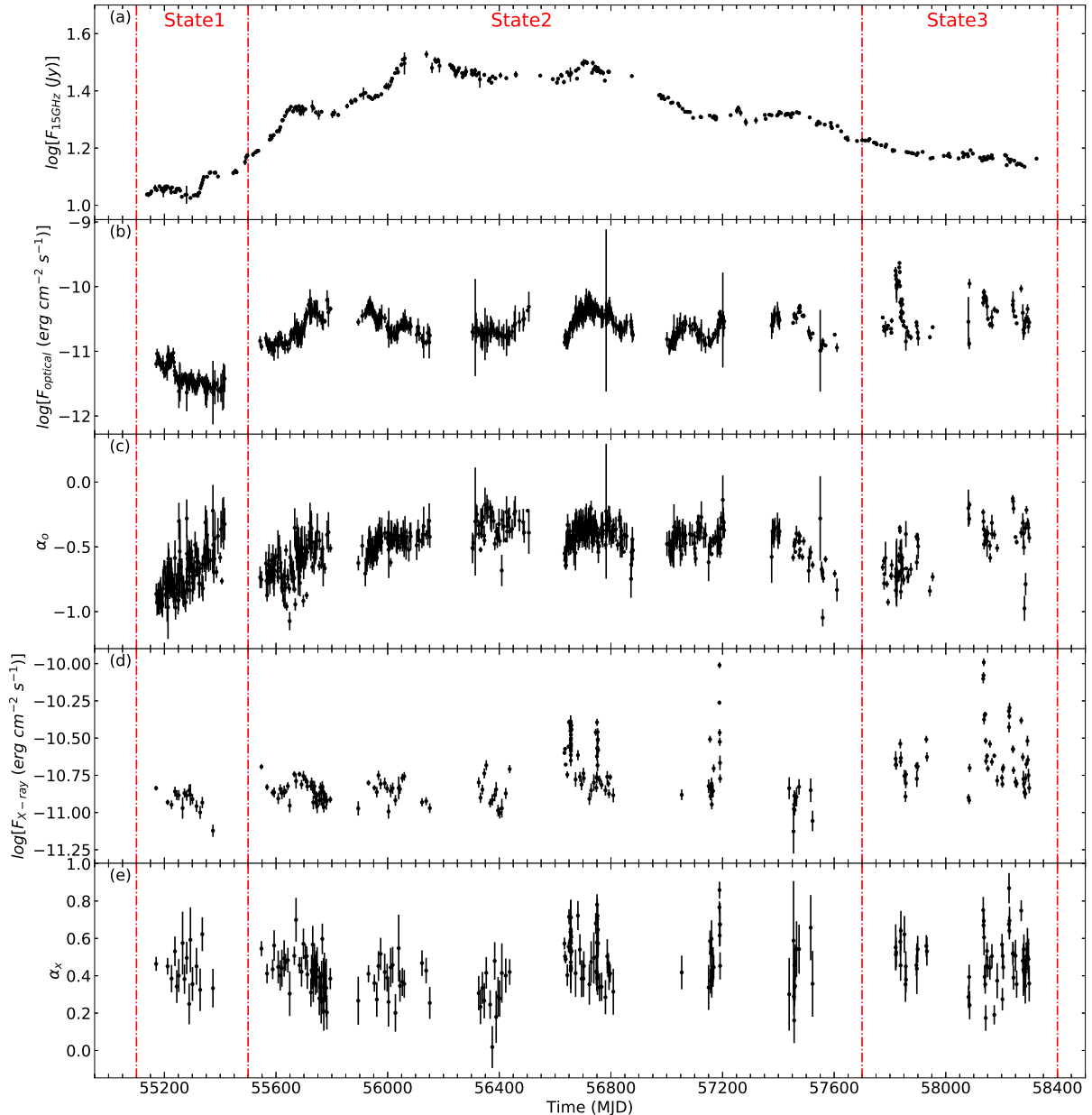


Figure 1. Multi-frequency light curves of 3C 279: (a): OVRO 15 GHz flux, (b): optical flux, (c): optical spectral index, (d): X-ray flux, and (e): X-ray spectral index. Vertical lines denote the time intervals for the states 1, 2, and 3 (see text), and the radio light curve is shown for reference.

show the 15 GHz radio light curve obtained in the OVRO catalog (Richards et al. 2011) for reference (Fig. 1 a).

2.3. Time-series SED fitting

Although the narrow-band fluxes (i.e., each observation) provided important insights into blazar jets previously (e.g., Larionov et al. 2020; Prince 2020), variability in the spectral shape cannot be studied in details with this approach. Since spectral shapes can be measured only with multi-frequency data, we combine the

data together to construct time series of the spectra in the optical and X-ray bands.

For each of these bands, we combine the data within one day and construct SEDs in each of the wavebands. Using slightly different time bins (e.g., 2–3 days) does not significantly alter the results presented below. Note that when we compare quantities measured by *Swift*/XRT, we do not bin the data in time.

We fit the optical SEDs with power-law models $K(\nu/\nu_0)^\alpha$, where ν_0 is the pivot frequency taken to be the geometric mean of the fit band. We then measure the

“logarithmic” flux (F_o ; “flux” hereafter) and the spectral index (α_o). In order to ensure that the observational data cover a wide frequency range ($\nu_{\min}-\nu_{\max}$) in the fits, we require that $\log_{10}(\nu_{\max}/\nu_{\min})$ is greater than 0.4 for the optical data. This requirement does not have large impact on the fits since the observations cover the fit band well. We verify that the models reasonably represent the SEDs by visual inspection.

The optical-band fits are formally unacceptable with reduced $\chi_r^2 \gg 1$, meaning that the measurement uncertainties are underestimated and/or the simple power law is inadequate to fit the high-quality optical data; these will make the uncertainties on the model parameters incorrectly small. Although it is unclear what the poor fits should be ascribed to, we increase the measurement uncertainties by a factor so as to make the fit reduced $\chi_r^2 = 1$, which also increases the uncertainties in F_o and α_o . The results are displayed in Figure 1 (b and c). We note that the Pearson correlation coefficient and its Fisher transformation (Fisher 1915) we use below take into account the scatter in the data (e.g., F_o and α_o measurements), and so the measurement uncertainties are indirectly accounted for via the scatter. We verify the results obtained from the Fisher transformation using simulations when necessary (e.g., § 3.1).

The 0.3–10 keV X-ray data are separately fit in XSPEC (see §2.1), and we measure the logarithmic flux (F_x) and derive the SED slope ($\alpha_x = 2 - \Gamma_X$). We present the results in Figure 1 (d and e). The *WISE* data cover three $\Delta T \approx 1$ day epochs at MJDs 55205, 55379, and 55567, and reveal that the optical continuum SED might curve downwards below $\sim 10^{14}$ Hz at some epochs. The measured SED slopes are $-0.49 \pm 0.03/-0.78 \pm 0.13$, $-0.59 \pm 0.03/-0.59 \pm 0.12$, and $-0.72 \pm 0.04/-0.77 \pm 0.25$ for the *WISE*/optical data at MJDs 55205, 55379, and 55567, respectively.

3. OPTICAL-TO-X-RAY VARIABILITY OF 3C 279

The light curves in Figure 1 show various phenomena at the observed frequencies. Long-term (years) and short-term (months) variabilities are clearly seen in the light curves. Some flares are observed only in one pass-band (e.g., the X-ray flare at MJD 56750 and the optical flare at MJD 57830), while some others are observed in multiple wavebands (e.g., >MJD 58000). It is hard to explain all these observational diversities with an emission scenario, and thus we focus on some of the features and a one-zone scenario here (see also Paliya et al. 2015; Larionov et al. 2020; Prince 2020).

In one-zone blazar emission models, the low-energy (optical) and the high-energy (X-ray to gamma-ray) radiations are related as they are assumed to share the

Table 2. Summary of correlations between the spectral properties

Band1	Band2	Property	r_p	Sig. (σ_F)	N_{pair}
Full data (MJD 55100–58400):					
Optical	Optical	F_o/α_o	0.44	12.4	693
X-ray	X-ray	F_x/α_x	0.65	12.0	239
Optical	X-ray	F_o/F_x	0.48	7.0	175
Optical	X-ray	α_o/α_x	−0.04	0.5	175
State 1 (MJD 55100–55500):					
Optical	Optical	F_o/α_o	−0.61	7.7	121
X-ray	X-ray	F_x/α_x	0.14	0.5	16
Optical	X-ray	F_o/F_x	0.25	0.9	16
Optical	X-ray	α_o/α_x	0.04	0.1	16
State 2 (MJD 55500–57700):					
Optical	Optical	F_o/α_o	0.41	9.5	490
X-ray	X-ray	F_x/α_x	0.72	11.5	166
Optical	X-ray	F_o/F_x	0.18	1.9	115
Optical	X-ray	α_o/α_x	−0.08	0.9	115
State 3 (MJD 57700–58400):					
Optical	Optical	F_o/α_o	0.07	0.6	82
X-ray	X-ray	F_x/α_x	0.59	5.0	57
Optical	X-ray	F_o/F_x	0.54	3.9	44
Optical	X-ray	α_o/α_x	−0.07	0.5	44

emitting particles (i.e., electrons) in the same region (Abdo et al. 2010). Hence, correlation between optical and X-ray emission should exist, and we search the spectral data for such correlation. Here, we consider two spectral properties, flux (F_i) and spectral index (α_i) in the optical ($i = o$) and X-ray bands ($i = x$), which makes up four correlations: one correlation between the spectral properties in each band (2 total) and two cross-band correlations for each property (2 total). Note that this approach is slightly different from the previous ones (e.g., Patiño-Álvarez et al. 2018; Beaklini et al. 2019; Larionov et al. 2020; Prince 2020) in the sense that we use spectral indices as well and measure fluxes over broader bands which represent the continuum better.

3.1. Correlations within and across the wavebands

With the band-fit fluxes F_i ’s and spectral indices α_i ’s that we measured (§2.3), we calculate the Pearson correlation coefficients (r_p) for the four pairs. The significance (σ_F) for the correlation is computed with the Fisher transformation. The results are summarized in Table 2 and scatter plots are shown in Figure 2. We verify that the significance estimated by the Fisher transformation well represents the null hypothesis probability using simulations; i.e., the chance probabilities for uncorrelated random samples (drawn from the normal distribution) to show the r_p values in Table 2 correspond to σ_F ’s estimated by the Fisher transformation.

In the single-band correlation study, we find very significant (e.g., $\geq 5\sigma$) correlations in both bands (9-yr data). Although the optical flux F_o and spectral index

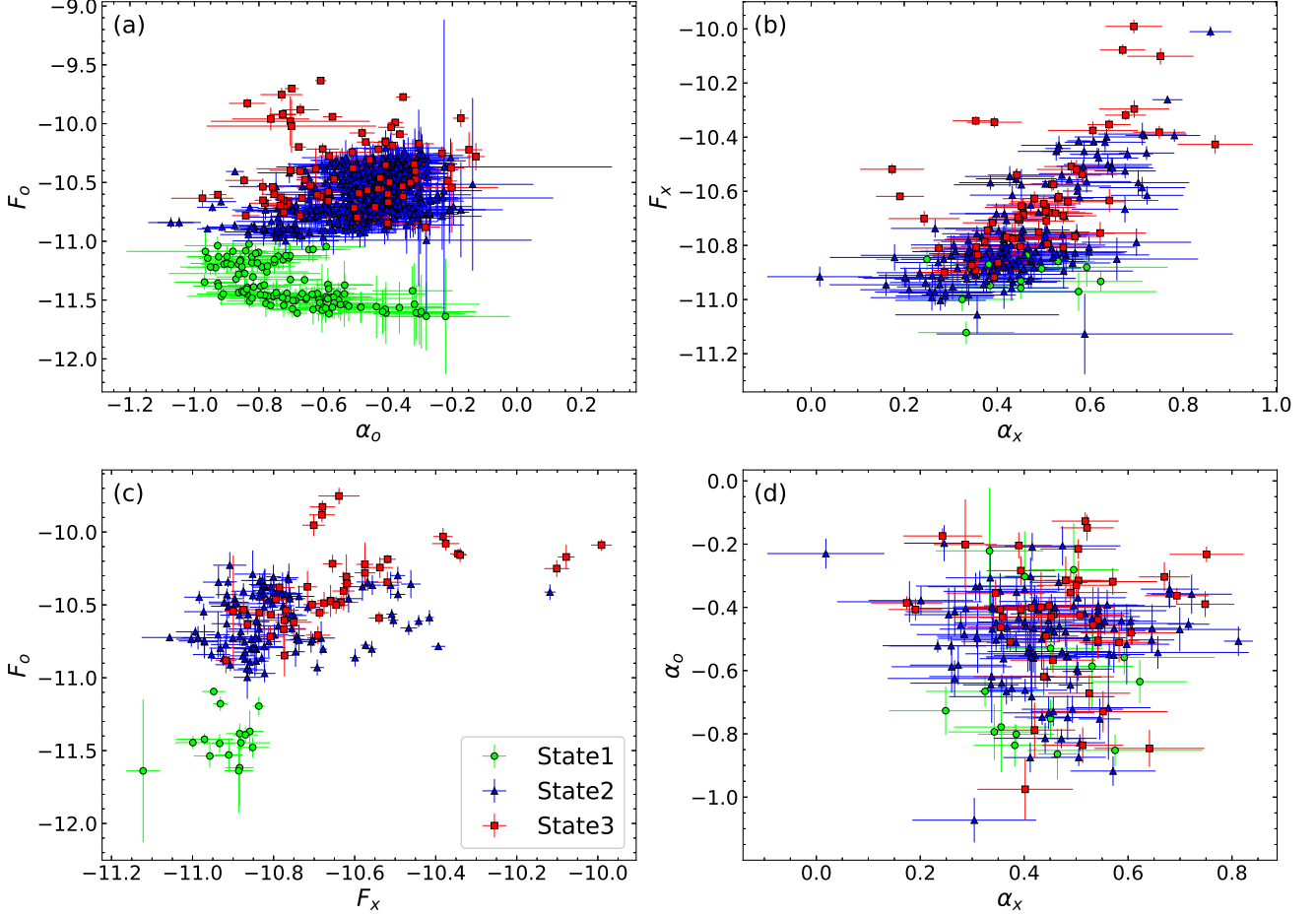


Figure 2. Scatter plots of the fit fluxes and spectral indices to show correlation within and across the wavebands. Correlations between F_i and α_i within a waveband are shown in the top row: optical (a) and X-ray (b) bands. Cross-band correlations between the fit fluxes (c: F_o-F_x) and between the spectral indices (d: $\alpha_o-\alpha_x$) are displayed in the bottom row. Data points for each state are denoted in color: green circle for state 1, blue triangle for state 2 and red square for state 3.

α_o show very significant correlation over the 9-yr period, it appears that there are two different “states” with dramatically different trends (i.e., negative and positive correlation) with a boundary at $F_o \approx -11$ (Fig. 2 a).

In the cross-band correlation study, we find significant correlations in F_o-F_x (Fig. 2 c; see also Larionov et al. 2020). Like the $F_o-\alpha_o$ case (see above), the F_o-F_x relation appears to form two groups depending on the F_o values (Fig. 2 c). In addition, light curves after MJD 57700 show more frequent activities at high energies, differing from the earlier ones. We therefore group the data into three states: (1) MJD 55100–55500 with low optical flux, (2) MJD 55500–57700 with high optical flux and mild activity, and (3) MJD 57700–58400 with high optical flux and strong activity. Note that the time intervals for these states are similar to those used by Larionov et al. (2020) based on the R -band and gamma-ray flux relations, but are slightly different from

theirs in that we do not use earlier data ($< \text{MJD } 55100$) and our state 3 includes their intervals 3 and 4.

The results for correlation studies in the states 1–3 are presented in Table 2. Note that the correlation in the F_o-F_x relation (Fig. 2 c) in the full data set almost disappears in states 1 and 2, and is weaker in state 3, meaning that the correlation in the full data set is primarily between the states (inter-state) rather than within them (intra-state) and that the correlation in state 3 is an intra-state one. While the inter-state correlations can tell us about the state transition of the blazar, we focus on the intra-state ones here.

3.2. Time-shifted Correlations

Because the cross-band correlation may be more significant with a time delay if emission in one band lags (leads) the other, we perform the same correlation study by shifting the data in time. This is essentially the same as the discrete correlation function

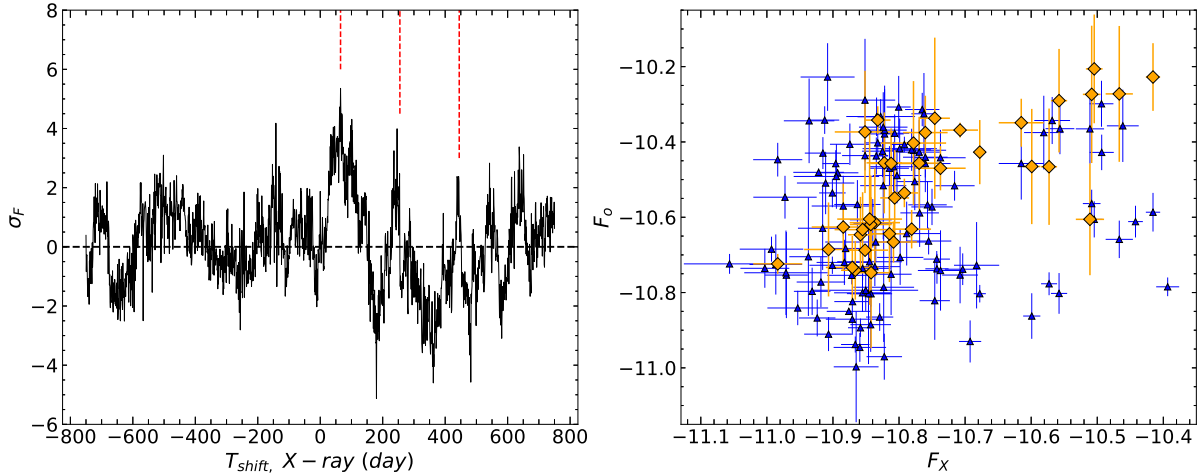


Figure 3. *Left:* significance plot for time-shift cross-band correlations between F_o and F_x in state 2. The x axis T_{shift} denotes the time shifts (1-day steps) and the shifted data with the positive values for X-ray lead. Negative y values mean anti-correlation. Red vertical lines mark 65 day, 255 day, and 445 day. *Right:* the corresponding scatter plot with F_x shifted by 65 days (orange diamond). Unshifted data are overlaid in blue triangle for reference.

(DCF; [Lioudakis et al. 2018](#), for example) method except that our data are binned. We compare cross-band properties in pairs of the two wavebands by shifting one of the data in time and measure the correlation significance (σ_F) as a function of the time shift (T_{shift} ; 1-day step). The results are consistent with those in Table 2; the time-shifted plots corresponding to the significant (cross-band) ones in the table show a prominent peak at $T_{\text{shift}} = 0$.

However, we find that F_o and F_x in state 2, whose correlation was insignificant without a time shift (Table 2), show significant correlation when one of them is shifted in time ($r_p = 0.73$ and $\sigma_F \approx 5.4$ at ~ 65 days; Fig. 3 left). As noted above (§ 3.1), σ_F well represents the null hypothesis probability, and so the false alarm probability for the correlation with the 65-day delay (pre-trial $\sigma_F = 5.4$) is $p = 6 \times 10^{-5}$ after considering 1,500 trials (i.e., $\sim 4\sigma$ post-trial). A similar delay of 64 day found in MJD 56400–56850 by an independent study ([Patiño-Álvarez et al. 2018](#)) enhances the significance for the shifted correlation. In our new analysis of the data, we find that this delayed correlation in state 2 (MJD 55500–57700) is stronger over the whole period of the state than in a part of it (e.g., MJD 56400–56850; [Patiño-Álvarez et al. 2018](#)), implying that the delay persisted for a longer period (e.g., the whole state). We also note that Figure 3 seems to show a possible periodic trend with a period of 190 days (red vertical lines in the left panel). This is intriguing, but significance for the later peaks is low. The periodic trend in the figure might appear just by chance.

For the time-shifted $F_o - F_x$ correlation in state 2, we show the scatter plots of the shifted (orange diamond)

and unshifted data (blue triangle) in Figure 3 right. In this state, there were several X-ray flares (Fig. 1) which can be seen as high-flux outliers in Figure 3 right. Since the source would have different emission properties during the flare periods from the low-flux quiescent ones (e.g., [Hayashida et al. 2015](#)), we check to see if the delayed correlation exists in the quiescent and flare periods separately. Because of the paucity of data points in flare, we investigate the quiescent periods only. We remove the high-flux outliers (i.e., taking $F_x \leq -10.75$), and compute r_p and its significance which are ≈ 0.65 and $\sigma_F \approx 4$, respectively.

4. INTERPRETATION OF THE SPECTRAL CORRELATION USING A TOY SED MODEL

In this section, we present our explanation on the observed variabilities using a simple one-zone scenario.

4.1. A Toy SED model

In order to explain the spectral correlations we found above, we construct a toy one-zone SED model using a leptonic synchro-Compton scenario (Fig. 4; see also [Sahayanathan & Godambe 2012](#); [Dermer et al. 2014](#); [Paliya et al. 2015](#), for example). In this work, we do not attempt to strictly match the highly-variable observational SEDs of 3C 279 with the toy model, but it is constructed so as to capture the main features of the SED and the relevant ingredients in blazar emission for our investigation of the spectral correlations; the figure is intended to be used only to guide eyes. The model and time-averaged SED data are shown in Figure 4, where the error bars on the optical and X-ray data points are standard deviation of the 9-yr flux measurements at the

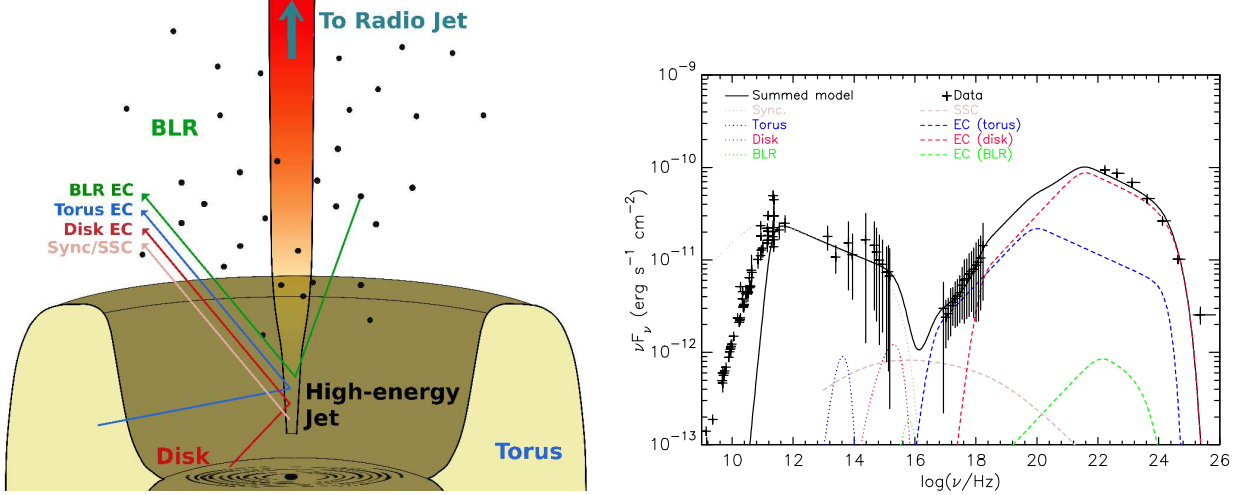


Figure 4. A schematic view of blazars' emission components (left; not to scale), and a toy one-zone SED model and time-averaged SED data (right). The optical and X-ray data points are measured in this work (collected over ~ 9 years), and the error bars on the data points are the standard deviation of the measurements. The radio and gamma-ray points are taken from the *vizier* catalog and the 4FGL catalog (8-year average), respectively. The summed model is displayed with a solid black line and each model component is denoted in color. Note that the synchrotron component (brown dotted) is shown without SSA to be compared to a model with SSA (black solid).

observed frequencies. Note that the gamma-ray SED is obtained from the 4FGL catalog (Abdollahi et al. 2020) and is a mission-averaged one, and the radio data are taken from the *vizier* photometry webpage.³

In this model, the optical SED is explained with the synchrotron radiation (brown dotted) of a broken power-law electron distribution ($dN_e/d\gamma_e \propto \gamma_e^{-p_1}$ with $p_1 = 3.3$ if $\gamma_e \geq 50$ and $p_1 = 2.3$ otherwise) and weak disk emission at the high-frequency end (red dotted). The spectral indices for the electron distribution are chosen so as to match the optical SED displayed in Figure 4 right and are similar to those expected in shock acceleration theories (e.g., Jones & Ellison 1991) and radiative cooling. The disk emission is computed following the standard Shakura-Sunyaev model for $M_{\text{BH}} = 5 \times 10^8 M_\odot$ (Shakura & Sunyaev 1973). Emissions of a torus and a broad line region (BLR) are included as blackbody radiation (e.g., Joshi et al. 2014); our investigation below does not strongly depend on the exact emission properties of these components (e.g., the emission frequency and spectral shape). We also show the SSC component (brown dashed) for reference but it may be even lower; given the observed shape of the average X-ray SED, this component cannot be significant. In the X-ray band, the emission is assumed to be produced by EC of torus (blue dashed) and disk photons (red dashed). Although the BLR EC is much weaker than the disk EC in our model, the converse is also possible if the jet locates closer to BLR/torus (e.g., Dermer 1995); BLR emitting

at slightly lower frequencies may replace the disk EC in the model.

Variability in this scenario can occur for various reasons: changes in internal conditions of the jet (e.g., particle spectrum N_e , magnetic-field strength B , the Doppler factor δ), location of the jet (i.e., EC efficiency), and change in the external seeds for EC (e.g., variable external emission u_{ext}). In the model, the frequencies and fluxes of the low-energy (synchrotron in the optical band) and the high-energy (EC in the X-ray to gamma-ray band) SED humps are related to the jet properties as in the following (e.g., Dermer 1995; An & Romani 2017):

$$\begin{aligned} \nu_{\text{SY}} &\propto \delta B \gamma_e^2, & F_{\text{SY}} &\propto B^{(1+p_1)/2} \delta^{(5+p_1)/2} \\ \nu_{\text{EC}} &\propto \delta^2 \gamma_e^2 \nu_{\text{ext}}, & F_{\text{EC}} &\propto \delta^{3+p_1} u_{\text{ext}}, \end{aligned}$$

where $\nu_{\text{SY,EC}}$ and $F_{\text{SY,EC}}$ are the observed (synchrotron and EC) emission frequency and flux, and ν_{ext} and u_{ext} are the emission frequency and flux of the external seeds for EC. Given the relatively straight power-law shape of the optical spectrum of 3C 279 (Fig. 4), the optical spectral index would not change much by δ and/or B (shifts of the SED) unless they vary a lot (e.g., orders of magnitude), in which case the flux would change even more. So variation of the optical spectral index (α_o) would be likely due to changes of the particle spectrum N_e with small contribution from δ and/or B .

Note that this model accounts only for the high-energy jet in which radio emission is highly suppressed by SSA (black solid vs. brown dotted lines). The radio emission is assumed to be produced in a separate parsec-scale 'radio' jet.

³ <http://vizier.unistra.fr/vizier/sed/>

4.2. State 1: MJD 55100–55500

In state 1 during which the optical flux is low, F_o – α_o shows negative correlation. No cross-band correlation is found. Although the changes of F_o and α_o may occur for various reasons as we noted above, the ‘negative’ F_o – α_o correlation may suggest that the change is stronger at low frequencies (i.e., soft), and can occur if N_e varies in the jet region.

A change of N_e would necessarily result in a corresponding change in the X-ray SED in one-zone scenarios; the optical and X-ray light curves (Fig. 1) show a hint of a correlated flux change (both drop with time), but the correlation is not significantly detected, perhaps because of the low statistics (16 pairs in this state). We verify this using simulations performed with correlated random samples and with the measured data; only $\leq 1\sigma$ detection of $r_p \approx 0.25$ correlation (e.g., F_o/F_x in Table 2) is possible with 16 pairs. Note that gamma-ray flux also drops in this state (e.g., Larionov et al. 2020). These imply that the soft-spectrum particles (N_e) were being removed from the high-energy emission region in this state. We may speculate that these particles move to the radio jets, thereby producing radio emission; the radio brightening in state 1 (Fig. 1) may support our speculation although the radio activity may be irrelevant to the optical one and was produced by a shock propagating in the radio jet (Hovatta et al. 2008) and/or independent changes in conditions in the radio jet: δ , B , and/or injection of particles.

4.3. State 2: MJD 55500–57700

In this state, properties within the bands are all positively correlated. In particular, the F_x – α_x correlation can give us strong constraints on the emission mechanism of the high-energy (\geq X-rays) radiation. This state overlaps very well with interval 2 of Larionov et al. (2020) in which the R-band (F_R) and gamma-ray (F_γ) flux relation of $F_\gamma \propto F_R^{7.7}$ is found. We note that the significant F_o – α_o correlation is primarily due to grouping of low-flux (e.g., $F_o \leq -10.8$) and high-flux points (blue points in Fig. 2 a); ignoring the low-flux ones reduces the significance rapidly. This indicates that state 2 may be further split, but the low-flux points do not localize in time. Therefore, we do not further split this state and regard that the F_o – α_o correlation is less significant (e.g., $\sim 3.8\sigma$ for $F_o \geq -10.8$).

Aside from the radio variability, observational properties in this state are that (1) $F_\gamma \propto F_R^{7.7}$, (2) F_x and α_x show “positively” correlated variability, implying that the disk EC varies more than the torus EC does, (3) F_x leads F_o by ~ 65 days (Fig. 3 left), and (4) variability in the optical spectral index implies N_e variation. Be-

cause $F_{EC}/F_{SY} \propto \delta^{\frac{1+p_1}{2}} u_{\text{ext}}/B^{\frac{1+p_1}{2}}$, changes of δ , B (by a factor of ≤ 3), and/or u_{ext} can explain (1). However, (2) is hard to be produced by the internal properties δ and B (e.g., α_x variability), and therefore we can conclude that u_{ext} is the primary source of the X-ray and hence gamma-ray variability. Furthermore, (3) cannot be explained by changes in the internal properties of the jet either because these will change the X-ray emission instantaneously (i.e., no delay).

Although the enhanced X-ray and gamma-ray emission should be driven by an increase in the external disk seed photons (u_{ext}), the ‘delayed’ optical emission (3) cannot be produced by the external sources themselves (e.g., disk) whose emission is much weaker than the synchrotron continuum (e.g., Fig. 4) and will ‘lead’ the reprocessed (upscattered) X-rays. Therefore, we speculate that the disk (external) activity responsible for (1) and (2) might enhance the optical continuum emission ~ 65 days later by synchrotron radiation in the ‘jet’; perhaps enhanced injection from the disk to the jet is responsible for this.

The ‘delayed’ optical variability (synchrotron) is natural in this scenario as N_e would vary by injection, but then the X-ray flux should also increase simultaneously by EC of the same N_e . Then F_x – F_o correlation with no delay in addition to the 65-day shifted one is expected but we do not see correlation without a delay (e.g., Fig 3 left). Perhaps, F_x variability induced by the injection into the jet (N_e) is swamped by the 65-day earlier disk EC activity (u_{ext}). Alternatively, the ‘delayed’ optical continuum variability (synchrotron in the jet) may be driven mainly by changes of B which affect F_o but not F_x . Indeed, the change of the optical flux (a factor of ~ 4) is larger than that of the X-ray one (a factor of ~ 2 ignoring large X-ray flux points $F_x \geq -10.8$ induced by flares; Fig. 3 right), suggesting that B may be the dominant factor (over N_e) for the delayed optical variability.

4.4. State 3: MJD 57700–58400

This state shows rapid and large variability in the high-energy band, suggesting that 3C 279 was active. Since our spectral data do not cover this time interval well, highly significant (e.g., $\geq 5\sigma$) correlation is found only between F_x and α_x (Table 2 and red square points in Fig. 2 b), implying that the disk EC is still variable. If the disk EC is the main driver of the high-energy variability, a strong F_γ – F_R trend as in state 2 is expected. However, Larionov et al. (2020) reported a weaker $F_\gamma \propto F_R^{1.9}$ trend in this state. This implies that the optical continuum emission also varied with the X-ray one; fairly significant $4\text{-}\sigma$ F_o – F_x correlation (Table 2) also suggests this (see also Prince 2020).

Provided that the optical flux is dominated by the synchrotron continuum radiation, it is likely that changes of N_e and δ are the main driver of the variability in this state. Assuming that B is constant and $p_1 \approx 2.3$, we find $F_{\text{EC}} \propto F_{\text{SY}}^{1.5}$, similar to $F_\gamma \propto F_R^{1.9}$ trend. Hence the variability in this state can be explained by changes of δ and N_e (spectral shape change in the optical band) with relatively weak disk EC variability (F_x - α_x correlation).

5. SUMMARY AND CONCLUSION

We investigated multi-frequency variability in the emission of the blazar 3C 279 using *Swift* UVOT/XRT, and various catalog data. We produced multi-band spectra and analyzed them in order to infer physical properties and emission mechanisms of the jet. We constructed time-resolved SEDs in the two wavebands, carried out spectral correlation studies, and found several significant correlations between the spectral properties within and across the wavebands. Note that variability in 3C 279 emission is much more complicated and may differ in each flare activity (e.g., Paliya et al. 2015; Hayashida et al. 2015), and that the correlations we found represent the overall properties of the 3C 279 jet.

In these spectral studies, we found that the F_o - α_o correlation exhibits a strong inversion, and therefore we split the data into three states based on the F_o - α_o correlation and activity in the light curves. We then investigated correlation properties in each state and interpret the results using a one-zone synchro-Compton scenario. Below are the summary:

- State 1: the F_o - α_o anti-correlation and a mild flux drop in the optical to gamma-ray band with time suggest that soft-spectrum particles (N_e) are lost from the high-energy jet.
- State 2: the $F_\gamma \propto F_R^{7.7}$ relation (Larionov et al. 2020) and F_x - α_x correlation imply that the disk-EC emission is variable due to some activity in the disk. Then the ~ 65 -day lag of F_o with respect to F_x and variability in the optical spectral index suggest that the activity in the disk might inject particles N_e and B into the high-energy jet on a time scale of ~ 65 days.
- State 3: F_x - α_x correlation again implies variability in the disk EC, and the F_o - F_x correlation and the $F_\gamma \propto F_R^{1.9}$ relation suggest that it is δ that mainly drives the variability in this state with some contribution of N_e and disk EC.

If it is the disk EC emission that drives the variability at X-rays in state 2 as we argued above, a 65-day delay of

the optical emission with respect to the gamma-ray one is also expected in state 2 and was seen in the earlier part of the state (Patiño-Álvarez et al. 2018). This implies that the emission mechanisms for X-rays and gamma rays are the same as in our SED model (Fig. 4).

It is interesting to note that the near “quiescent” state (state 1), a short period (~ 400 days) after large radio activity (e.g., Chatterjee et al. 2008), is followed by active states (states 2 and 3) in which injection of N_e and changes of B/δ occur. The time interval is coincident with new long-term radio activity, and it is worth investigating whether and how the high-energy (\geq optical) states are related to the radio activity. Investigations of high-energy data taken during previous and future long-term radio activity may be very intriguing.

Because 3C 279 is very bright and frequently observed, high-quality multi-band data exist. Using only small part of the observational data and a one-zone SED scenario, we were able to suggest that the emission mechanism for the high-energy SED hump is the tours and disk EC, and explore causes of the spectral variability. Although the one-zone model can explain the results obtained in this work, the source exhibits enormously diverse spectral variability that cannot be explained with the model. More data (e.g., time-varying broadband SEDs) and improved SED models can certainly provide very useful information. In this regard, we acknowledge that our interpretation is speculative rather than definitive. Further comprehensive data analyses (e.g., including polarization and gamma-ray emission; Abdo et al. 2010) and theoretical studies (e.g., magnetohydrodynamic simulations and multi-zone SED models) are warranted to advance our knowledge on 3C 279, and blazars in general.

ACKNOWLEDGMENTS

We thank the anonymous referee for the careful reading of the paper and insightful comments. This research has made use of data from the OVRO 40-m monitoring program (Richards et al. 2011) which is supported in part by NASA grants NNX08AW31G, NNX11A043G, and NNX14AQ89G and NSF grants AST-0808050 and AST-1109911. This publication makes use of data products from the Wide-field Infrared Survey Explorer, which is a joint project of the University of California, Los Angeles, and the Jet Propulsion Laboratory/California Institute of Technology, funded by the National Aeronautics and Space Administration. Data from the Steward Observatory spectropolarimetric monitoring project were used. This program is supported by Fermi Guest Investigator grants NNX08AW56G, NNX09AU10G, NNX12AO93G, and NNX15AU81G. This paper has made use of up-to-date SMARTS optical/near-infrared light curves that are available at www.astro.yale.edu/smarts/glast/home.php. We acknowledge the use of public data from the *Swift* data archive. This research was supported by Basic Science Research Program through the National Research Foundation of Korea (NRF) funded by the Ministry of Science, ICT & Future Planning (NRF-2017R1C1B2004566).

Facilities: OVRO, *WISE*, Steward, SMARTS, *Swift*

Software: HEASoft (v6.22; HEASARC 2014), XSPEC (Arnaud 1996)

REFERENCES

- Abdo, A. A., Ackermann, M., Ajello, M., et al. 2010, *Nature*, 463, 919
- Abdollahi, S., Acero, F., Ackermann, M., et al. 2020, *ApJS*, 247, 33
- Ackermann, M., Ajello, M., An, H., et al. 2016, *ApJ*, 820, 72
- An, H., & Romani, R. W. 2017, *ApJ*, 838, 145
- . 2018, *ApJ*, 856, 105
- Anders, E., & Grevesse, N. 1989, *GeoCoA*, 53, 197
- Arnaud, K. A. 1996, in *Astronomical Society of the Pacific Conference Series*, Vol. 101, *Astronomical Data Analysis Software and Systems V*, ed. G. H. Jacoby & J. Barnes, 17
- Beaklini, P. P. B., Dominici, T. P., Abraham, Z., & Motter, J. C. 2019, *A&A*, 626, A78
- Bessell, M. S., Castelli, F., & Plez, B. 1998, *A&A*, 333, 231
- Blandford, R. D., & Znajek, R. L. 1977, *MNRAS*, 179, 433
- Bonning, E., Urry, C. M., Bailyn, C., et al. 2012, *ApJ*, 756, 13
- Bottacini, E., Böttcher, M., Pian, E., & Collmar, W. 2016, *ApJ*, 832, 17
- Böttcher, M., Reimer, A., Sweeney, K., & Prakash, A. 2013, *ApJ*, 768, 54
- Chatterjee, R., Jorstad, S. G., Marscher, A. P., et al. 2008, *ApJ*, 689, 79
- Dermer, C. D. 1995, *ApJL*, 446, L63
- Dermer, C. D., Cerruti, M., Lott, B., Boisson, C., & Zech, A. 2014, *ApJ*, 782, 82
- Fisher, R. A. 1915, *Biometrika*, 10, 507
- H. E. S. S. Collaboration, Abramowski, A., Acero, F., et al. 2013, *A&A*, 550, A4
- Hayashida, M., Nalewajko, K., Madejski, G. M., et al. 2015, *ApJ*, 807, 79
- Hovatta, T., Nieppola, E., Tornikoski, M., et al. 2008, *A&A*, 485, 51
- Jones, F. C., & Ellison, D. C. 1991, *SSRv*, 58, 259
- Joshi, M., Marscher, A. P., & Böttcher, M. 2014, *ApJ*, 785, 132

- Larionov, V. M., Jorstad, S. G., Marscher, A. P., et al. 2020, *MNRAS*, 492, 3829
- Liodakis, I., Romani, R. W., Filippenko, A. V., et al. 2018, *MNRAS*, 480, 5517
- MacDonald, N. R., Marscher, A. P., Jorstad, S. G., & Joshi, M. 2015, *ApJ*, 804, 111
- Marziani, P., Sulentic, J. W., Dultzin-Hacyan, D., Calvani, M., & Moles, M. 1996, *ApJS*, 104, 37
- Paliya, V. S., Sahayanathan, S., & Stalin, C. S. 2015, *ApJ*, 803, 15
- Patiño-Álvarez, V. M., Fernandes, S., Chavushyan, V., et al. 2018, *MNRAS*, 479, 2037
- Prince, R. 2020, *ApJ*, 890, 164
- Richards, J. L., Max-Moerbeck, W., Pavlidou, V., et al. 2011, *ApJS*, 194, 29
- Rodrigues, X., Fedynitch, A., Gao, S., Boncioli, D., & Winter, W. 2018, *ApJ*, 854, 54
- Romani, R. W., Sowards-Emmerd, D., Greenhill, L., & Michelson, P. 2004, *ApJL*, 610, L9
- Sahayanathan, S., & Godambe, S. 2012, *MNRAS*, 419, 1660
- Schlafly, E. F., & Finkbeiner, D. P. 2011, *ApJ*, 737, 103
- Shakura, N. I., & Sunyaev, R. A. 1973, *A&A*, 500, 33
- Smith, P. S., Montiel, E., Rightley, S., et al. 2009, *arXiv e-prints*, arXiv:0912.3621
- Urry, C. M., & Padovani, P. 1995, *PASP*, 107, 803
- Verner, D. A., Ferland, G. J., Korista, K. T., & Yakovlev, D. G. 1996, *ApJ*, 465, 487